102ħk Large Area Atom Interferometers

Sheng-wey Chiow, Tim Kovachy, Hui-Chun Chien, and Mark A. Kasevich

102$\hbar$k Large Area Atom Interferometers

Sheng-wey Chiow, Tim Kovachy, Hui-Chun Chien and Mark A. Kasevich

Department of Physics, Stanford University, Stanford, California 94305, USA

Abstract

We demonstrate atom interferometers utilizing a novel beam splitter based on sequential multi-photon Bragg diffractions. With this sequential Bragg large momentum transfer (SB-LMT) beam splitter, we achieve high contrast atom interferometers with momentum splittings of up to 102 photon recoil momenta (102$\hbar k$). To our knowledge, this is the highest momentum splitting achieved in any atom interferometer, advancing the state-of-the-art by an order of magnitude. We also demonstrate strong noise correlation between two simultaneous SB-LMT interferometers, which alleviates the need for ultra-low noise lasers and ultra-stable inertial environments in some future applications. Our method is intrinsically scalable and can be used to dramatically increase the sensitivity of atom interferometers in a wide range of applications, including inertial sensing, measuring the fine structure constant, and detecting gravitational waves.

PACS numbers: 03.75.Be, 03.75.Dg, 37.25.+k, 06.30.Gv

Atom interferometry has proven to be a powerful tool for precision metrology [1]. Light-pulse atom interferometers [2, 3], which use two-photon Raman transitions as beam splitters ($\pi/2$-pulses) and mirrors (π-pulses) for the atoms, have demonstrated the capability to be precise inertial sensors [4–7] and to precisely measure the fine structure constant [8]. Additionally, atom interferometry is a promising means to test general relativity [9] and to detect gravitational waves [10, 11].

The full potential of atom interferometric sensors has yet to be realized due to the relatively modest performance of the existing atom optics: the sensitivity of an atom interferometer typically scales linearly with the space-time area enclosed by the interferometer [1], whereas two-photon Raman transitions provide momentum separation of only 2 photon recoils of momentum ($2\hbar k$, where k is the wavenumber of the light). A long-standing goal has been to increase the interferometer area through the use of beam splitters that transfer many photon recoils of momentum. Such beam splitters have been achieved by applying sequential two-photon Raman transitions [12] and alternatively by applying a single multi-photon Bragg diffraction [13]. However, the degree to which these methods are scalable has been limited by population loss for a large number of two-photon Raman pulses and by the prohibitive intensity requirements for higher order Bragg pulses [14]. Another promising method for achieving scalable beam splitters involves transferring momentum to the atoms through Bloch oscillations in an optical lattice [15–18]. This approach, however, currently reaches $24\hbar k$ and is limited mainly by the spatial extent of the atomic cloud and the wavefront distortion of the beams.

In this work, we demonstrate that appropriately configured sequences of optical pulses used in conjunction with evaporatively cooled ensembles of atoms can be used to realize very large momentum transfer atom optics. In particular, we demonstrate coherent atom optics capable of delivering nearly 1 m/s velocity kicks to atomic wavepackets, corresponding to a momentum transfer of $102\hbar k$.

We operate a Mach-Zehnder interferometer consisting of an initial beam splitter sequence to split a cold cloud from a Bose-Einstein Condensate (BEC) into two wavepackets with different momenta, a mirror sequence to redirect the wavepackets toward each other, and a final beam splitter sequence to interfere the wavepackets (Fig. 1a). The use of a BEC atom source mitigates interference contrast loss from transverse and longitudinal atom source velocity spread. Each beam splitter and mirror sequence is a composite of a number of
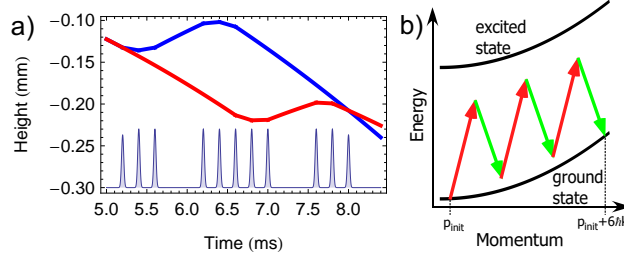
FIG. 1: (color online) a) Depiction of a sample pulse sequence and the corresponding trajectories of the interfering wavepackets. The thick lines illustrate the wavepacket trajectories, while the thin line in the bottom portion of the figure represents the temporal intensity profile of the pulse sequence. This particular sequence has SB-LMT beam splitters consisting of three $6\hbar k$ pulses, corresponding to a total momentum splitting of $18\hbar k$. The first and final pulses of the sequence are $\pi/2$-pulses, and the middle nine pulses are π-pulses. Each pulse has a Gaussian temporal profile. b) The energy-momentum diagram of $6\hbar k$ Bragg transition driven by two counter-propagating beams (green and red).

multi-photon Bragg pulses (sequential Bragg large momentum transfer, SB-LMT), with the first and last pulses of the interferometer being $\pi/2$-pulses and the rest being π-pulses [19]. An nth order multi-photon Bragg pulse can be understood as a $2n$-photon process that couples two momentum states separated by $2n\hbar k$, creating an effective two-level system (Fig. 1b) [20]. Figure 2 shows an image of the two wavepackets after a $30\hbar k$ SB-LMT beam splitter and an image of a single wavepacket given a $30\hbar k$ momentum kick.

To produce the BECs, we use the apparatus described in [24–26]. Approximately 10^8 ^{87}Rb atoms are loaded into a time-orbiting potential (TOP) trap. Evaporative cooling yields a BEC of ~ 3000 atoms in the $|F = 2, m_F = 2\rangle$ state with temperature ~ 4 nK. The atoms are detected using absorption imaging with a CCD camera. The spatial resolution of the imaging system is 2.5 μm, allowing us to clearly resolve populations in different momentum states using time-of-flight imaging. To minimize the effect of stray magnetic fields on the atoms, we transfer the population into the $|F = 2, m_F = 0\rangle$ state with 50% efficiency with a 3.8 μs, 1.35 MHz rf pulse in the adiabatically relaxed TOP trap. After switching off the TOP trap, the population in other Zeeman states is pulled away from the interferometer interrogation region by magnetic dipole forces by a short current pulse in the quadrupole magnetic coils. At the beginning of the interferometer sequence, the cloud has $1/e$ radius

FIG. 2: (color online) a) Absorption image of the cloud after the application of a $30\hbar k$ SB-LMT beam splitter. The beam splitter consists of five sequential $6\hbar k$ pulses (one $\pi/2$-pulse, four π-pulses). The image is taken after 4 ms time-of-flight from the application of the first pulse, corresponding to a wavepacket separation of 600 μm. The faint spots between the two main wavepackets arise from pulse inefficiency due to imperfections. b) Image of the cloud after the application of five consecutive $6\hbar k$ π-pulses, effectively forming a $30\hbar k$ SB-LMT π-pulse. Each $6\hbar k$ π-pulse has an efficiency of 94%, corresponding to a total efficiency of $\sim 73\%$ for the five pulse sequence. False color red corresponds to a higher atom density [21]. The images in this figure have been rotated by 90 degrees.

~ 8 μm. (Note that the $30\hbar k$ and $102\hbar k$ interferometer sequences described below do not start at identical delays from the cloud generation).

To generate the laser beams for the atoms optics, we use the fiber-coupled output of a tunable Titanium-sapphire laser having ~ 300 mW output power. The laser beam is split evenly into two paths, each of which passes through an acousto-optic modulator (AOM) to adjust the frequency offset and amplitude. The two paths are directed so as to respectively form the downward (top beam) and upward (bottom beam) propagating atom optics beams. The offset frequencies of the top beam (f_1) and the bottom beam (f_2) are controlled by an FPGA-controlled direct digital synthesizer (DDS) system.

The atom optics beams have Gaussian spatial profiles with waists of 1.5 mm, and with lin∥lin polarization configuration. We adjust the power coupled through the fiber so that the top (bottom) beam contains approximately 100 mW of power before being diffracted by the AOM. The laser frequency is tuned between 27 GHz and 200 GHz below the 780 nm D_2 ($F = 2 \rightarrow F' = 3$) transition. We use closer detunings for higher order Bragg pulses, which require larger two-photon Rabi frequencies [14, 27, 28].

We shape the Bragg pulses to have Gaussian temporal profiles by shaping the amplitude at which we drive the AOMs with an AFG3102 Tektronix arbitrary function generator (AFG). A variable attenuator (Mini-Circuits ZAS-3) allows us to separately control the

4

AOM frequencies and amplitudes with inputs from the DDS and the AFG, respectively. The use of Gaussian pulses instead of square pulses allows for a significantly improved transfer efficiency [13, 14].

The sequences we implement use individual Bragg pulses that transfer 6-20 $\hbar k$ of momentum, with sequential pulses spaced by 200 μs. The full width half maximum (FWHM) of each pulse is $\sim$ 100 μs. To specify whether a particular pulse is a π-pulse or a $\pi/2$-pulse, we set its amplitude appropriately. We chirp f_1 to compensate for gravity, and we use piecewise adjustments of f_2 to set each pulse to be on resonance with the targeted wavepacket.

Using SB-LMT beam splitters and mirrors consisting of 6$\hbar k$ pulses, we realize interferometers with momentum splittings of up to 102$\hbar k$, an order of magnitude increase over previous atom interferometers [13, 17]. For the 102$\hbar k$ interferometer, each SB-LMT beam splitter consists of 17 pulses, and the mirror sequence consists of 33 pulses. Mainly due to the vibration of the folding mirror $\sim$ 1 m above the optical table, laser phase noise is too large to allowing us to scan an interference fringe, which in the absence of such noise could be achieved by systematically varying the chirp rate of f_1 and observing the corresponding oscillations in the difference between the populations in the two output ports (6$\hbar k$ and 0$\hbar k$ momentum states) of the interferometer. In our case, laser phase noise is large enough to drive full amplitude fluctuations of this population difference with the chirp rate of f_1 held constant. By observing the amplitude of these fluctuations, we can estimate the contrast of the interferometer, which is the maximum observed value of the normalized population difference between the two output ports. Fig. 3 show images illustrating the population fluctuating between the two interferometer output ports for 30$\hbar k$ and 102$\hbar k$ interferometers, respectively. Fig. 3e shows the $\sim$ 5% diffraction efficiency fluctuation of a $\pi/2$ pulse. In a full interferometer, this leads to an inferred $\sim$ 1% fluctuation in the normalized population difference between the outputs [29], which is a small effect compared to the observed $\sim$ 20% fluctuation for a 102$\hbar k$ interferometer. A histogram depicting the distribution of this $\sim$ 20% fluctuation is shown in Fig. 3f. This distribution is consistent with a sinusoidal fringe with randomly varying phase from shot to shot. The respective maximum wavepacket separations for the 30$\hbar k$ and 102$\hbar k$ interferometers are 200 μm and 2 mm.

With 30$\hbar k$ beam splitters we observe 70% contrast. Even with 102$\hbar k$ beam splitters, we observe a contrast of 18%, which is significantly better than previous work with 24$\hbar k$ beam splitters [13]. The increase in contrast is due to the narrow velocity distribution of our cloud,
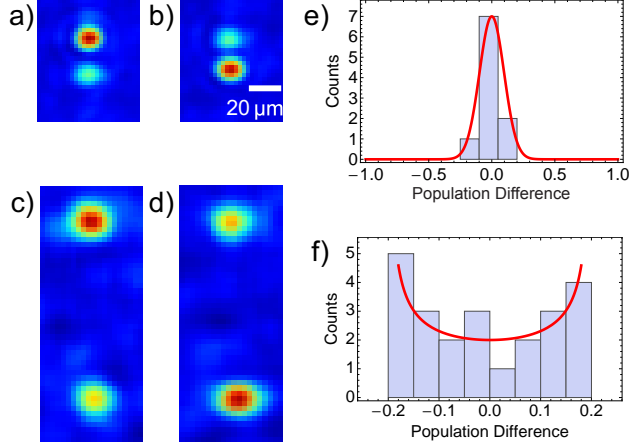
FIG. 3: (color online) a)–d) Examples of typical data showing images of the two interferometer output ports. a) and b) correspond to an interferometer with $30\hbar k$ SB-LMT beam splitters, while c) and d) correspond to an interferometer with $102\hbar k$ SB-LMT beam splitters. The fact that the atom clouds for the $102\hbar k$ interferometer are slightly larger than the clouds for the $30\hbar k$ interferometer is due to the fact that the detection time was later for the $102\hbar k$ interferometer than for the $30\hbar k$ interferometer (respectively 21 ms and 12 ms after the production of the cold cloud, so that in each case the atoms would return to our imaging region at the time of detection), which gives the clouds more time to thermally expand. e) Histogram of population difference of single $\pi/2$-pulse and a normal distribution with 5% diffraction efficiency variation (standard deviation). f) Histogram of population difference of a $102\hbar k$ interferometer, and a synthesized distribution of an interferometer output with 18% contrast and randomly varying phase from shot to shot (red curve). The $30\hbar k$ interferometer output has a similar distribution with 70% contrast.

which results in high transfer efficiency, and to the small cloud size, which reduces influences from wavefront distortions. Nevertheless, wavefront distortions are likely responsible for the fact that we see less than full contrast with $102\hbar k$ SB-LMT beam splitters. As discussed in detail in [11], wavefront distortions can lead to a spatially dependent interferometer phase shift across the cloud. For instance, for $102\hbar k$ beam splitters, a wavefront distortion across the atom cloud of magnitude $\sim \lambda/100$ leads to a spatially dependent phase of magnitude $\sim 2\pi$. Note that the contribution of wavefront distortions to the interferometer phase shift is coupled to the transverse motion of the atoms, since in the absence of any transverse motion the phase imparted by wavefront distortions would cancel as a common mode between the two arms of the interferometer. The effects of wavefront distortions are proportional to the

number N of photon recoils transferred to the atoms, which is consistent with the fact that the observed contrast is lower for $102\hbar k$ SB-LMT beam splitters. A top view of the cloud would allow us to resolve the resulting spatially dependent interference pattern—however, since we image the cloud from the side, we see an apparent decrease in contrast.

For this work, the momentum separation we can achieve in an interferometer is not limited by the degradation of contrast, but rather by population loss. We observe that the maximum efficiency per photon recoil transferred is achieved by using $6\hbar k$ pulses. Each $6\hbar k$ π-pulse has an efficiency of 94% (which is $\sim 99\%$ per $\hbar k$), leaving us with $0.94^{34} \sim 10\%$ of the original atom number after a $102\hbar k$ interferometer, since each arm of the interferometer undergoes 34 pulses. We believe that the inefficiency is due to the instability of the two-photon Rabi frequency. We expect that in future experiments the diffraction efficiency can be improved by implementing robust laser frequency and intensity stabilization feedback loops, and by individually optimizing the parameters of each pulse [30]. We do not observe significant diffraction efficiency change over this range of population difference, which indicates that the mean field shift [31] is not a concern in our case. Note also that fluctuations in the mean field shift from shot to shot can cause noise in the output phase of an interferometer or in the differential phase between two conjugate interferometers. Given our estimated mean field-induced frequency shift of ~ 10 Hz and our interferometer interrogation times of ~ 10 ms, this does not currently limit us (see discussion below). The use of dense samples in this work is dictated by our detection scheme, and in future work, dilute ensembles can be used to mitigate mean field effects (including phase diffusion [32]).

Common mode noise cancellation between simultaneous interferometers is used to take advantage of the extraordinary sensitivity of LMT atom optics while providing immunity from vibration-induced phase noise [5, 33]. Here, we implement simultaneous interferometers with $30\hbar k$ SB-LMT beam splitters to demonstrate the noise cancellation capability of SB-LMT. For the $30\hbar k$ SB-LMT interferometer, in addition to the previously mentioned nearly full contrast, enough atoms remain after the interferometer sequence to allow us to divide the initial population into two simultaneous, topologically identical interferometers separated vertically by ~ 70 μm: a single $6\hbar k$ $\pi/2$-pulse splits the sample into two clouds, which subsequently spatially separate during a drift time of 2 ms. After this drift time, we apply the interferometer pulse sequence. Since the two interferometers are addressed by the same laser beams, the contributions from laser phase noise and from accelerations (*e.g.*, gravity)
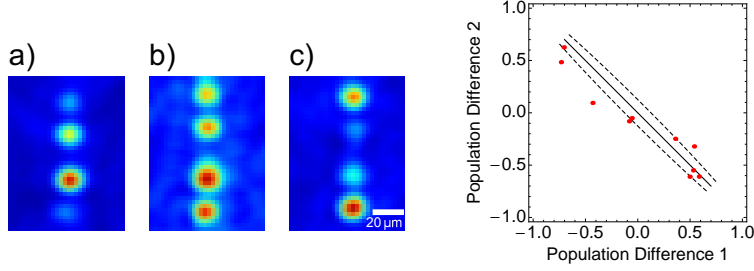
FIG. 4: (color online) Parametric plot of simultaneous $30\hbar k$ interferometer outputs. The upper interferometer output is plotted on the x-axis while the lower interferometer is plotted on the y-axis. The off-diagonal line shows the expected correlation between two simultaneous interferometers having phase difference π with 70% contrast, and the dashed curves show the atom shot noise (there are 250 atoms per interferometer at the time of detection). a)–c) Typical images at various relative phases. The lower spots correspond to the two output ports of the lower interferometer, while the upper spots correspond to the two output ports of the upper interferometer.

to the difference $\Delta\phi_{\mathrm{upper}} - \Delta\phi_{\mathrm{lower}}$ between the phase shifts of the two interferometers cancels as a common mode [34]. The difference $\Delta\phi_{\mathrm{upper}} - \Delta\phi_{\mathrm{lower}}$ is sensitive to the local gravity gradient [5, 6], but in our case this contribution is too small to be resolved due to the short baseline separating the two interferometers. Thus, the lone non-negligible contribution to $\Delta\phi_{\mathrm{upper}} - \Delta\phi_{\mathrm{lower}}$ arises from the fact that initial populations for the two interferometers occupy two different input ports. Namely, the population in the upper interferometer is initially in state $|6\hbar k\rangle$, while the population in the lower interferometer is initially in state $|0\hbar k\rangle$, so that $\Delta\phi_{\mathrm{upper}} - \Delta\phi_{\mathrm{lower}} = \pi$. Our data are consistent with this result—that is, we observe the respective population differences of the $6\hbar k$ and $0\hbar k$ output ports of the two interferometers fluctuating out of phase, as shown in Fig. 4. This demonstrates that the common mode cancellation of laser phase noise works as expected for SB-LMT beam splitters. This common mode cancellation is crucial to future experiments with large-area atom interferometers, such as those proposed in [10, 11]. As indicated in Fig. 4, the common mode noise cancellation works well enough so that fluctuations in $\Delta\phi_{\mathrm{upper}} - \Delta\phi_{\mathrm{lower}}$ occur at the level of atom shot noise. Future work will explore the limitations and requirements of the common mode noise cancellation [6, 10, 11].

To put our results into perspective, we consider their implications for several future experiments. The 10 m atomic fountain at Stanford will allow for pulse spacings of ~ 1 s [3],

which with $\sim 100\hbar k$ beam splitters corresponds to meter-scale wavepacket separations. With a flux of 10^6 atoms/s, the shot-noise-limited acceleration sensitivity of such an interferometer is $\sim 10^{-13}$g/$\sqrt{\text{Hz}}$, surpassing the current state-of-the-art by multiple orders of magnitude [4, 35]. Moreover, $\sim 100\hbar k$ beam splitters can allow for highly sensitive inertial sensors that can fit in a spatially compact interrogation region, making them readily transportable outside of the laboratory. For instance, with ~ 30 ms pulse spacings, a signal to noise ratio of 100:1 per shot, and one shot per second, an accelerometer with sensitivity $\sim 10^{-9}$g/$\sqrt{\text{Hz}}$ could be achieved with a ~ 1 cm interrogation region. Also, by using an interferometer geometry analogous to that described in [33] with $\sim 100\hbar k$ beam splitters, ~ 1 s pulse spacings, and a flux of 10^6 atoms/s, a shot-noise-limited measurement of h/m_{Rb} would have a sensitivity of $\sim 10^{-12}h/m_{\text{Rb}}$ /$\sqrt{\text{Hz}}$, allowing for a greatly improved determination of the fine structure constant [8, 33]. In addition, the proposed AGIS-LEO mission, which will use satellite-based atom interferometers in low-Earth orbit to detect gravitational waves, requires $\sim 100\hbar k$ beam splitters to reach its design sensitivity [11]. Our realization of such beam splitters in the laboratory is thus an important milestone in this effort. Finally, with technical improvements such as better wavefront quality, brighter atom sources, and higher pulse efficiency, we see no impediments to scaling this method to larger momentum transfer, perhaps in excess of $1000\hbar k$.

[1] *Atom Interferometry*, edited by P. R. Berman (Academic Press, New York, 1997); A. D. Cronin, J. Schmiedmayer, and D. E. Pritchard, Rev. Mod. Phys. **81**, 1051 (2009).

[2] C. J. Bordé, Phys. Lett. A **140**, 10 (1989).

[3] J. M. Hogan, D. M. S. Johnson, and M. A. Kasevich, P. Int. Sch. Phys **168**, 411 (2009).

[4] A. Peters, K. Y. Chung, and S. Chu, Metrologia **38**, 25 (2001).

[5] M. J. Snadden, J. M. McGuirk, P. Bouyer, K. G. Haritos, and M. A. Kasevich, Phys. Rev. Lett. **81**, 971 (1998).

[6] J. M. McGuirk, G. T. Foster, J. B. Fixler, M. J. Snadden, and M. A. Kasevich, Phys. Rev. A **65**, 033608 (2002).

[7] T. L. Gustavson, P. Bouyer, and M. A. Kasevich, Phys. Rev. Lett. **78**, 2046 (1997).

[8] R. Bouchendira, P. Cladé, S. Guellati-Khélifa, F. Nez, and F. Biraben, Phys. Rev. Lett. **106**, 080801 (2011).

[9] S. Dimopoulos, P. W. Graham, J. M. Hogan, and M. A. Kasevich, Phys. Rev. D **78**, 042003 (2008).

[10] S. Dimopoulos, P. W. Graham, J. M. Hogan, M. A. Kasevich, and S. Rajendran, Phys. Rev. D **78**, 122002 (2008).

[11] J. M. Hogan, D. M. S. Johnson, S. Dickerson, T. Kovachy, A. Sugarbaker, S.-w. Chiow, P. W. Graham, M. A. Kasevich, B. Saif, S. Rajendran, P. Bouyer, B. D. Seery, L. Feinberg, and R. Keski-Kuha, Gen. Relativ. Gravit. **43**, 1953 (2011).

[12] J. M. McGuirk, M. J. Snadden, and M. A. Kasevich, Phys. Rev. Lett. **85**, 4498 (2000).

[13] H. Müller, S.-w. Chiow, Q. Long, S. Herrmann, and S. Chu, Phys. Rev. Lett. **100**, 180405 (2008).

[14] H. Müller, S.-w. Chiow, and S. Chu, Phys. Rev. A **77**, 023609 (2008).

[15] J. Hecker Denschlag, J. E. Simsarian, H Häffner, C. McKenzie, A. Browaeys, D. Cho, K. Helmerson, S. L. Rolston, and W. D. Phillips, J. Phys. B. **35**, 3095 (2002).

[16] P. Cladé, S. Guellati-Khélifa, F. Nez, and F. Biraben, Phys. Rev. Lett. **102**, 240402 (2009).

[17] H. Müller, S.-w. Chiow, S. Herrmann, and S. Chu, Phys. Rev. Lett. **102**, 240403 (2009).

[18] T. Kovachy, J. M. Hogan, D. M. S. Johnson, and M. A. Kasevich, Phys. Rev. A **82**, 013638 (2010).

[19] Specifically, where j is a positive integer, the initial beam splitter sequence consists of a single $\pi/2$-pulse followed by $j-1$ π-pulses. The $\pi/2$-pulse splits the cloud into two wavepackets, while the π-pulses accelerate the diffracted wavepacket upward. The mirror sequence consists of $2j-1$ π-pulses, the first half of which decelerate the upper wavepacket and the latter half of which accelerate the lower wavepacket. The final beam splitter sequence consists of $j-1$ π-pulses to decelerate the lower wavepacket followed by a single $\pi/2$-pulse to recombine and interfere the two wavepackets. If each Bragg pulse transfers n photon recoils ($n\hbar k$), then the total momentum splitting between the arms is $N\hbar k$, where $N = j \times n$.

[20] M. Kozuma, L. Deng, E. W. Hagley, J. Wen, R. Lutwak, K. Helmerson, S. L. Rolston, and W. D. Phillips, Phys. Rev. Lett. **82**, 871 (1999).

[21] To remove some of the imaging noise (due to, for example, stray light and vibration of the imaging optics), images are passed through a Principal Component Analysis filter [22, 23].

Subsequently, we smooth the images by convoluting them with a 4 pixel by 4 pixel square kernel.

[22] I. T. Jollife, *Principal Component Analysis* (Springer, New York, 2002).

[23] S. R. Segal, Q. Diot, E. A. Cornell, A. A. Zozulya, and D. Z. Anderson, Phys. Rev. A **81**, 053601 (2010).

[24] W. Li, A. K. Tuchman, H.-C. Chien, and M. A. Kasevich, Phys. Rev. Lett. **98**, 040402 (2007).

[25] B. P. Anderson, Ph.D. thesis, Stanford University, 2000.

[26] C. Orzel, A. K. Tuchman, M. L. Fenselau, M. Yasuda, and M. A. Kasevich, Science **291**, 2386 (2001).

[27] P. J. Martin, B. G. Oldaker, A. H. Miklich, and D. E. Pritchard, Phys. Rev. Lett. **60**, 515 (1988).

[28] D. M. Giltner, R. W. McGowan, and S. A. Lee, Phys. Rev. Lett. **75**, 2638 (1995).

[29] Where the first $\pi/2$-pulse has efficiency P_1 and the second $\pi/2$-pulse has efficiency P_2, the normalized population difference between the two output ports (in the absence of interference) is $(1 - 2P_1)(1 - 2P_2)$. For the pulse efficiencies P_1 and P_2 nominally equal to 50%, 5% fluctuations in the pulse efficiencies lead to fluctuations in the normalized population difference of $0.1 \times 0.1 = 1\%$.

[30] Such improvement is important since the atom shot noise limited sensitivity of an interferometer increases as the square root of the number of atoms remaining at the end of the interferometer sequence.

[31] J. Stenger, S. Inouye, A. P. Chikkatur, D. M. Stamper-Kurn, D. E. Pritchard, and W. Ketterle, Phys. Rev. Lett. **82**, 4569 (1999).

[32] A. Imamoglu, M. Lewenstein, and L. You, Phys. Rev. Lett. **78**, 2511 (1997); W. Li, A. K. Tuchman, H.-C. Chien, and M. A. Kasevich, Phys. Rev. Lett. **98**, 040402 (2007).

[33] S.-w. Chiow, S. Herrmann, S. Chu, and H. Müller, Phys. Rev. Lett. **103**, 050402 (2009).

[34] Here each readout phase $\Delta\phi$ is defined so that the population difference of the corresponding $6\hbar k$ and $0\hbar k$ output ports varies as $C \sin \Delta\phi$, where C is the contrast.

[35] H. Müller, S.-w. Chiow, S. Herrmann, S. Chu, and K. Y. Chung, Phys. Rev. Lett. **100**, 031101 (2008).